# Comparison between Distributed Acoustic Sensing and Geophones: Downhole Microseismic Monitoring of the FORGE Geothermal Experiment

Ariel Lellouch*[1], Nathaniel J. Lindsey[1], William L. Ellsworth[1], and Biondo L. Biondi[1]

## Abstract

**We compare the performance of a downhole distributed acoustic sensing (DAS) fiber-optic array with that of conventional geophones. The downhole collocated arrays are part of the Frontier Observatory for Research in Geothermal Energy (FORGE) geothermal experiment, in which stimulation of the rock volume in an enhanced geothermal system (EGS) causes microseismic events. The DAS acquisition system yields data sampled at every 1 m at 2000 samples per second for the entire length of the well, spanning to a depth of 985 m from the surface. Whereas single DAS channels are substantially noisier than geophones at the same location, their large number and spatial coherency allow for the application of effective array processing techniques. We follow a complete workflow for the fiber-optic array: velocity model building, event detection, event location, and magnitude estimation. Estimated velocity models agree well with sonic logging in a nearby well and map a granitic contact accurately. Detection performance is somewhat worse than geophones and yields magnitude completeness of −1.4 compared to −1.7 for geophones. Using a single vertical fiber array, we cannot retrieve the azimuth of the events relative to the well. However, we can very accurately estimate their depth and horizontal distance from the array. Magnitude estimation with DAS approaches geophone results to within a standard deviation of $M = 0.115$ and negligible mean difference. The DAS processing results outperform a regional and local surface array, consolidated with a shallow borehole sensor. Although downhole geophones in the FORGE experimental layout performed better, DAS holds several critical practical benefits that were not demonstrated. Thanks to its heat resistance, it can be deployed much closer to the reservoir; fibers can be deployed along cased active wells, eliminating the need for a dedicated monitoring well; the permanently installed fiber can be used for years or decades. Therefore, we argue that DAS holds vast potential for long-term monitoring of EGS projects.**

**Cite this article as** Lellouch, A., N. J. Lindsey, W. L. Ellsworth, and B. L. Biondi (2020). Comparison between Distributed Acoustic Sensing and Geophones: Downhole Microseismic Monitoring of the FORGE Geothermal Experiment, *Seismol. Res. Lett.* **XX**, 1–13, doi: 10.1785/0220200149.

## Introduction

The stimulation of the rock matrix by pressurized injection of fluid is the underlying technology behind unconventional hydrocarbon recovery and enhanced geothermal systems (EGS), in which the target is opening new or activating existing fractures. EGS can be economical only if permeable fracture networks that can sustain substantial heat-accumulating fluid flow from injection to production well without short circuiting are created (Majer *et al.*, 2007). Because of the increased pressure, fractures in the rock can open, reactivate, or enlarge. During stimulation, the monitoring of microseismic earthquakes (magnitude $\mathbf{M} < 0$) provides information about the developing fracture network. If the seismic monitoring array is deployed very close to the stimulation area, it is feasible to detect events with magnitudes as low as $\mathbf{M} - 3$ (Maxwell, 2014). These events are subsequently located and undergo magnitude and, depending on the acquisition geometry and data quality, focal mechanism inversion to determine the likely orientation of the fault plane. The combined information provided by the monitoring array is used to estimate the stimulated volume, track the fracture network to avoid structural hazards and groundwater contamination, improve the

1. Geophysics Department, Stanford University, Stanford, California, U.S.A.
*Corresponding author: ariellel@stanford.edu

understanding of the reservoir connectivity and barriers, and influence production decisions.

In microseismic analysis for hydrocarbon recovery projects, downhole geophone arrays are the state-of-the-art (Maxwell *et al.*, 2012). However, drilling dedicated monitoring wells incurs substantial additional costs, and operators often resort to deploying surface arrays only. Although such arrays can detect induced seismicity, their effectiveness for the much weaker microseismic events is limited in terms of detection, location, magnitude estimation, and focal mechanism reconstruction (Eisner *et al.*, 2009, 2010; Chambers *et al.*, 2010, 2014).

To compare various seismic technologies, one can use the signal-to-noise ratio (SNR) in the microseismic frequency band, which can depend on the local site noise and individual sensor instrument self-noise, but ultimately represents a system's sensitivity and performance. For example, Earth noise decreases away from the free surface; thus, well-based sensors have higher SNR. However, there are many additional capabilities beyond SNR that should be considered when designing a system for microseismic monitoring. For example, arrays of sensors are capable of retrieving seismic wavefield information, such as *P*- and *S*-wave velocities, by moveout analysis, and also can be used to identify sharp lithological contrasts from direct observation of seismic conversions. In an array, the designed sensor spacing and density often depend on the coherence length of the seismic wavefield, but sometimes a large aperture is more important than unaliased recording. The sensor housing may also be a crucial capability in higher temperature and pressure conditions or when the experiment's duration spans months to years, for example, in applications of induced seismicity monitoring in carbon sequestration or EGS.

An enticing alternative to deploying geophones in a monitoring well is to utilize the distributed acoustic sensing (DAS) technology. In DAS, an optical fiber can be used as a seismic sensor when interrogated by a dedicated system. In the oil and gas industry, downhole deployments of DAS arrays have been conducted for almost a decade (Mateeva *et al.*, 2013, 2014; Jin and Roy, 2017; Karrenbach *et al.*, 2019). They have been used for active seismic surveys, microseismic monitoring, and low-frequency strain measurements. DAS has several benefits for EGS monitoring. First, the fibers can be deployed behind casing, thus permitting other operations in the well to go undisturbed. Perforation and stimulation technologies allow for operating in fiber-instrumented cased wells (Lellouch, Horne, *et al.*, 2019), thus potentially transforming either the stimulating or production well into a monitoring one, and eliminating the need for a dedicated, separate monitoring well. Noise levels in an active well will be higher, mostly due to tube waves, but they can be handled through processing steps. Operating in uncased active fluid-filled wells is also possible at the cost of a further decrease in SNR (Kimura *et al.*, 2019; Uematsu *et al.*, 2019). Fibers with appropriate coating are also resistant to typical reservoir temperature and pressure conditions and can thus be deployed much closer to the reservoir than conventional downhole sensors (Zhidong *et al.*, 2019). Because the precise understanding of the fracture network created by stimulation is critical for successful EGS projects, deploying a high-resolution DAS fiber very close to the microseismic events could potentially become a game changer. Finally, fibers can be left underground for years. As such, they are ideal for long-term monitoring and time-lapse studies. Although chemical processes, especially "hydrogen darkening," can degrade fiber quality during long-term exposure to high temperatures, different methods are being developed to address this limitation (Chalifoux and Logan, 2009).

DAS systems are inherently different from geophones and seismometers. Depending on the particular optoelectronic setup of the DAS instrument, distributed measurements of strain rate or strain are collected in the direction of the fiber with a temporal resolution of 1–100 kHz. A single DAS sensor is a virtual channel of which sampling in space is determined by the discretization of the optical signal recorded at one end of the fiber, commonly 1–10 m. A modern DAS deployment usually includes thousands or tens of thousands of such sensors. DAS sensors are essentially uniaxial strainmeters and have strong directivity effects for different seismic phases (Benioff, 1935; Martin *et al.*, 2018). Although complex helically wound fiber designs aim to recover a more uniform response (Lim Chen Ning and Sava, 2018), they are not widely used in downhole acquisitions. Currently, single DAS channels have lower SNR than geophones (Daley *et al.*, 2016; Wang *et al.*, 2018), but their number and extent can compensate for this shortcoming in terms of array processing. In addition, the frequency response of DAS is far more broadband than typical inertial geophones with flat response down to 0.008 Hz or lower (Becker and Coleman, 2019; Lindsey *et al.*, 2020). There are many more technical details to DAS acquisition and processing, most notably their gauge length and the optical-phase unwrapping process (Parker *et al.*, 2014; Dean *et al.*, 2016; Papp *et al.*, 2017).

Downhole DAS has been mostly used for microseismic monitoring of sources close to the array (Karrenbach *et al.*, 2017, 2019). In these cases, DAS is often installed along a deviated horizontal well. However, vertical DAS arrays recording relatively distant events have been shown useful for earthquake detection (Lellouch, Yuan, Ellsworth, *et al.*, 2019; Lellouch, Yuan, Spica, *et al.*, 2019). In this study, we apply a similar technique to microseismic monitoring of the Utah Frontier Observatory for Research in Geothermal Energy (FORGE) geothermal experiment. In addition to the *P*- and *S*- wave velocity model building and event detection, we extend the DAS analysis to include partial event location and magnitude estimation. Thanks to a colocated downhole geophone array operating in parallel to DAS, we can compare their performance and draw quantitative conclusions about the effectiveness of DAS in this configuration.

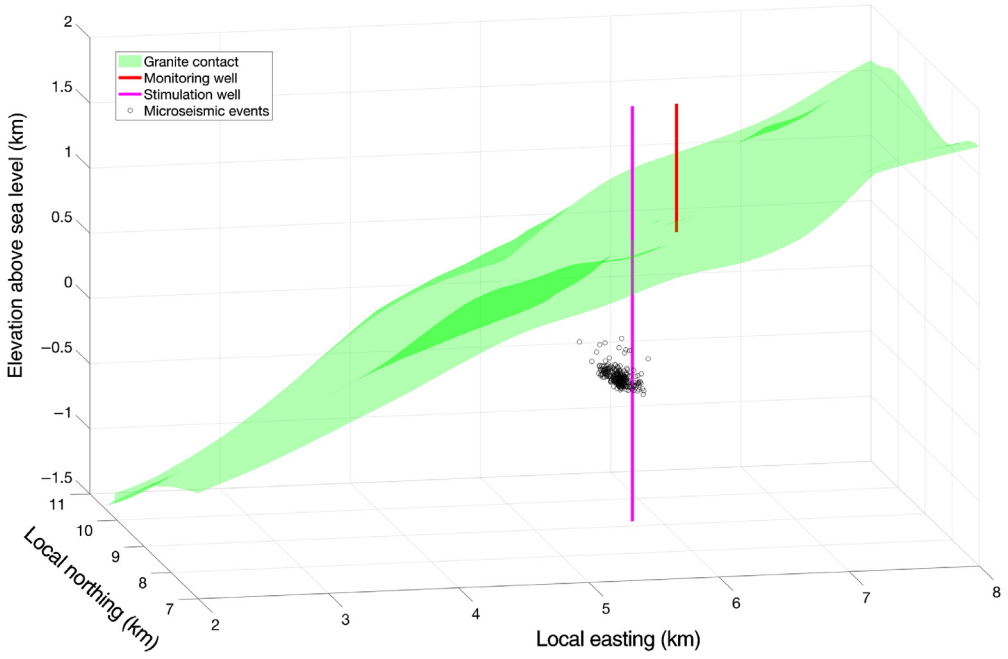


**Figure 1.** Geometry of the stimulation experiment. The mapped granite contact of the region is shown in dark green. The stimulating well (magenta) reaches about 2242 m deep from the surface. The monitoring well (red) spans to a depth of 985 m from the surface and crosses the granite contact. It is equipped with an optical fiber along its entire length and with a 12-level three-component (3-C) geophone array, covering the depth range of 645–980 m with a 30.5 m spacing between geophones. The microseismic locations obtained from the downhole geophones are plotted in black circles. The color version of this figure is available only in the electronic edition.

## Study Area and Monitoring Arrays

The U.S. Department of Energy FORGE is a dedicated underground field laboratory in Utah, purpose of which is to develop, test, and accelerate breakthroughs in EGS. FORGE is located near the town of Milford in Beaver County, Utah, on the western flank of the Mineral Mountains. Among the wells drilled at FORGE, well 58-32 was used for stimulation and well 78-32, located about 400 m east-southeast of 58-32, was used for deep seismic monitoring (see Fig. 1). We focus on the DAS and geophone array seismic data from well 78-32, but note that a few additional sensors were installed in an adjacent shallow well (68-32). Well 78-32 was equipped with an optical fiber in a metal tube, cemented behind the casing. The installed fiber was engineered by Silixa and interrogated using the Carina (Naldrett *et al.*, 2020) system. Engineered fibers are typically designed to improve the backscattered energy budget and have been shown to improve the optical measurement SNR by 10–20 dB (Correa *et al.*, 2017). DAS data have been acquired with a 1 m channel spacing using a 10 m gauge length and 2000 samples per second after 16-fold internal summation of the laser sampling rate. The output of the DAS interrogator is an optical-phase measurement of the strain rate, which can be converted from radians per second to physical strain rate (measured in nm/m per second) by a linear conversion.

Well 78-32 has also been equipped with an industry-grade 12-level geophone string deployed by Schlumberger. These geophones are positioned at depths of 645–980 m, with 30.5 m spacing between geophones. Geophones were only recording during stimulation intervals. We analyze the microseismic events generated by the stimulation of the geothermal reservoir. We focus on a highly active ~24 hr window, between 27 April 2019, 5 p.m. (UTC) and 28 April 2019, 5:10 p.m. (UTC). The microseismic catalog constructed from the downhole geophones by Schlumberger contains 299 events, estimated locations of which are also plotted in Figure 1, during this period. Because of proprietary information issues, we do not know the full details of the different steps taken during processing and thus use the downhole catalog as supplied by the contractor.

## Building *P*-Wave Velocity along the DAS Array

As mentioned, we follow the methodology of Lellouch, Yuan, Ellsworth, *et al.* (2019) for DAS-based event detection, which first requires the velocity profile along a vertical DAS well. There was no sonic logging in the monitoring well, and we thus need to estimate the velocity with another method. Lellouch, Yuan, Spica, *et al.* (2019) suggested using a slant-stack methodology applied to DAS records of vertically incident earthquake wavefields from source locations below the well. However, in this study, we have a known higher-frequency source—perforation shots. Hydraulic stimulation conducted in the well was preceded by two perforation shots. These perforations occur at a known location in the stimulation well. However, their timing is only known up to a 1 s precision. The perforation shots conducted in the stimulation well are located approximately 370 m (horizontally) and 1200 m (depth) away from the bottom of the monitoring well. We assume that seismic phases excited by the perforation propagate in an approximately uniform medium to the bottom of the monitoring array. This assumption is justifiable as all propagation is in the granitic basement, in which the seismic velocity is approximately uniform. Following straight-ray propagation, we find the perforation shots reach the bottom of the

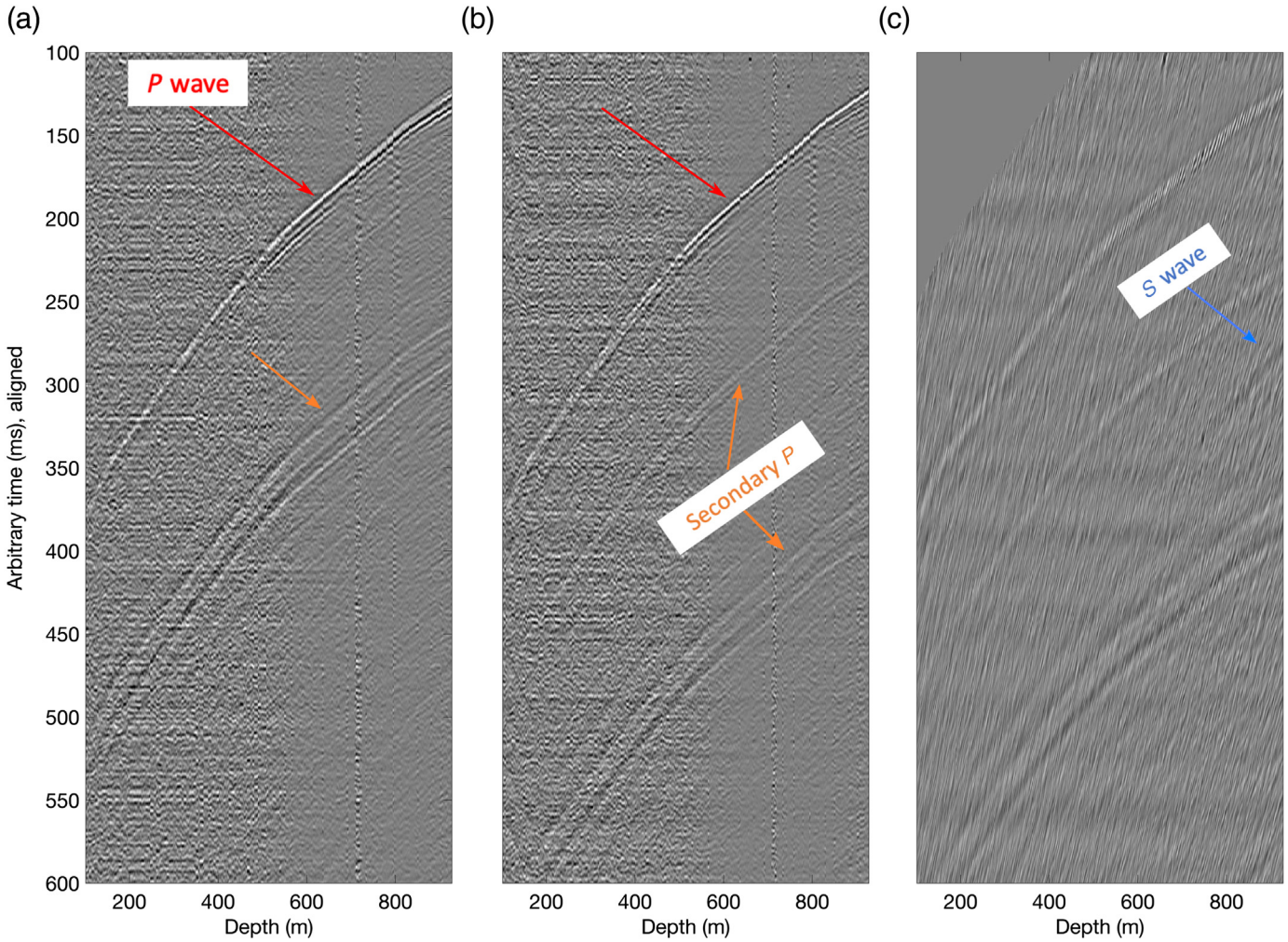


**Figure 2.** (a,b) Two perforation shots recorded in the distributed acoustic sensing (DAS) array. We manually align them by the first arrival *P* wave at the bottom of the array. The first arrival phase, marked in red arrows, is similar for the two perforations. However, secondary *P*-wave events, marked by orange arrows, and not used in this study, differ. No clear *S*-wave energy is present due to the perforation shot focal mechanism and DAS directivity. However, in panel (c), more extensive data processing of the perforation shot in panel (b) can unveil a weak *S* phase visible in the bottom of the array (blue arrow). The color version of this figure is available only in the electronic edition.

monitoring array at an incidence angle of about 20°. This angle is measured as relative to the vertical fiber axis, with 0° indicating upward propagation. After establishing the incidence angle at the bottom of the array, we follow the approach of Lellouch, Yuan, Spica, *et al.* (2019). In Figure 2, we show the two perforation shots. We first remove the median value of the array at each time sample and then bandpass the data between 10 and 250 Hz, which is a representative range of the frequency content for perforation shots. The median filtering step is essential, as it removes most of the interrogator imprint (laser drift, reference loop vibration, etc.). We also apply trace normalization for display purposes. The first *P*-wave arrivals are clear and consistent, and can be coherently followed along the entire array. *S*-wave arrivals are hardly visible. Nonetheless, with more intensive data processing, which contains $f$-$k$ velocity filtering and automatic gain control (Yilmaz, 2001), it is also possible to detect weaker *S* phases that have a distinctly different slope (Fig. 2c).

We use the first arrivals to estimate the local velocity along the array with a slant-stack decomposition applied to array subsets of 100 m range with a single channel overlap (Lellouch, Yuan, Spica, *et al.*, 2019). The same procedure is conducted for both perforation shots, and the results are eventually averaged. The velocity estimated in this fashion is only the local apparent velocity along the array (inverse vertical slowness). Because the perforations originated from the adjacent well at almost 400 m horizontal offset, seismic waves arrive at the DAS array subsets with a vertical slowness component that depends on their position along the array. However, this component is, by definition, smaller than for perfectly vertically upgoing waves. The apparent velocity is thus an overestimation of the actual subsurface *P*-wave velocity. Therefore, we apply an additional workflow to compensate for the angle of incidence. We again assume a constant angle of incidence below the granite contact. Because the

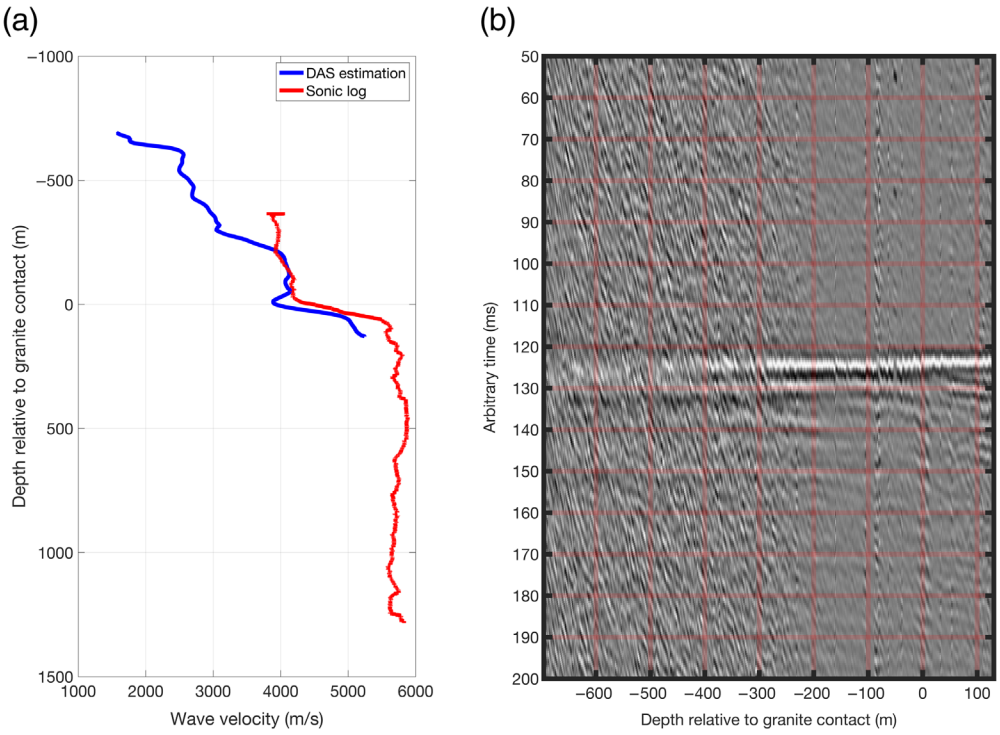


**Figure 3.** (a) Estimated *P*-wave velocity model (blue) compared to sonic logging in the stimulation well (red). The sonic log has been smoothed with a 90 m window. Both velocities are plotted as a function of depth distance from the estimated granite contact (Fig. 1). They are in good agreement far from the granite, and the sharp change of velocity occurs at the same depth. (b) Quality control of the DAS velocity model. The second perforation shot is aligned according to time lags computed from the DAS velocity model in panel (a) and a known angle of incidence. The record is flat, indicating that the velocity model we use is adequate. The color version of this figure is available only in the electronic edition.

velocity changes along the array above this depth, so does the angle of incidence. Therefore, we iteratively apply Snell's law, given a known angle of incidence at the bottom of the array and the initial velocity model estimation. This calculation yields the correct angle of incidence as a function of depth along the array with uncertainty we estimate at most at ±1°. Subsequently, we scale the apparent *P*-wave velocity estimates by the cosine of the depth-dependent angle to retrieve the *P*-wave phase velocity profile along the DAS array. We finally average the models estimated using the two perforation shots.

We show the result of this process in Figure 3a and compare it with sonic logging conducted in the stimulation well. We plot the velocity as a function of distance from the estimated granite contact. The granite surface mapping is only accurate for the stimulation well, and relies on interpolation and surface seismic for its estimation in the monitoring well location. Therefore, at the location of monitoring well 58-32, we use the estimated depth from the driller's log and completion report instead. DAS velocity estimation is in very good agreement with the sonic log. The sharp change in velocity, indicating the granite crossing, is aligned in depth. It is also important to note that the sonic log measures propagation velocities in entirely different frequencies, usually above the kilohertz range. Our method also averages rock properties over a broader depth range, because the slant-stack is applied over 100 m windows, compared to the spatially localized sonic logging. Nevertheless, we have confidence in our estimated *P*-wave velocity model at the location of well 78-32, because the perforation shots are aligned with the time lags predicted from the estimated DAS velocity model and the known angle of incidence (Fig. 3b shows the alignment of the second perforation shot). Recorded data are almost perfectly flattened, indicating that the velocity model we obtain is accurate for the frequency range of interest. Active survey surface-data processing in the area yielded a *P*-wave velocity structure (see Data and Resources), which after conversion from time to depth is very similar to the DAS estimation, albeit smoother and with lower resolution. Because the surface seismic processing was reflection-based time-domain processing, this is expected.

## Building an *S*-Wave Velocity Model

Recorded perforation shots do not contain significant *S*-wave energy and cannot be used to build an *S*-wave velocity model. However, microseismic events, which generate much stronger DAS-recorded shear energy, can be used to construct an *S*-wave velocity profile, given additional assumptions. If the estimated *P*-wave velocity model is reliable, we can measure the event's angle of incidence using the *P* phase. Because propagation from the source to the bottom of the array is entirely in the granitic basement, it is reasonable to assume the same angle of incidence for both *P* and *S* arrivals. This assumption is equivalent to stating that the Poisson's ratio is constant along the propagation path in the granite. Once this angle is known, we can repeat the process used to construct the *P*-wave velocity model from the perforation shots, but using the *S*-phase of the microseismic event. In Figure 4, we show a microseismic event that was used for *S*-wave velocity estimation. Because we

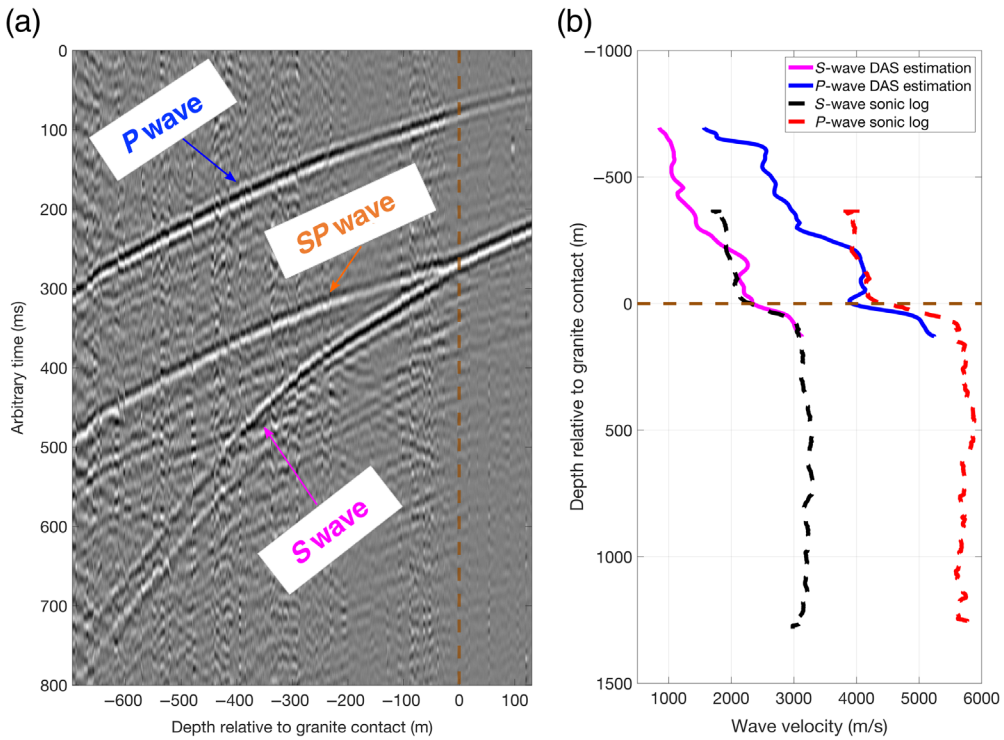


**Figure 4.** *S*-wave velocity model building. (a) A strong microseismic event (dated 27 April, 20:20:58 UTC) generating *S* waves, filtered in a 10–50 Hz range. There are direct *P* waves (blue arrow) used to estimate the angle of incidence. The *S* wave (magenta arrow) has a much steeper slope, indicating lower velocity. The granite contact is marked in dashed brown, and a clear *S*–*P* conversion (orange arrow) appears at its location. (b) Estimated *S*-wave velocity from DAS (magenta) and *S*-wave sonic logging (black). We smooth the sonic log with a 90 m window. We also plot the previously shown *P*-wave velocity models, estimated from DAS (blue) and sonic log (red). The agreement between DAS and sonic log estimation of *S* waves is excellent, and *P*- and *S*-velocity models computed from DAS follow the same structure. The granite contact is marked in dashed brown. The color version of this figure is available only in the electronic edition.

require high SNR, stronger microseismic events are useful. Nonetheless, their frequency content is often lower. In this example, we filter the data between 10 and 50 Hz, compared to 10–250 Hz for the perforation shots. The reconstructed *S*-wave model agrees well with the sonic log and has the same structure as that of the *P*-wave velocity inferred from the perforation shots. The sonic logs validate our assumption of approximately constant velocity in the granitic basement. The shallow structure also matches the results obtained by Zhang *et al.* (2019), using low-frequency ambient field measurements.

In the geometrical configuration of this study, it is impossible to construct velocity models using microseismic events only. The reason is that the angle of arrival for the microseismic events is in the range of 15°–20°. As such, it has a significant influence on the measured travel times. Had the angle been less than 10° (as in Lellouch, Yuan, Spica, *et al.*, 2019), we could have claimed that the effect is negligible anyhow, and the exact angle is not required. Because this is not the case, accurate knowledge of the angle of arrival is required to remove its imprint from the measured arrival times. Using a microseismic event only, the angle of arrival is unknown, and there is no way to decouple the influence of the true velocity model and angle of incidence on the measured travel times. This is the reason that a perforation shot of known location (or, not ideally, an estimation of the microseismic event location) is required.

## Comparison with Downhole Geophones

In the case of the FORGE EGS microseismic monitoring experiment, a downhole array of 12-level three-component (3-C) geophones spanning approximately 335 m was collocated in well 78-32 with a single-component vertical DAS fiber array of almost 1000 channels spanning the entire well. In this section, we compare these two sensor arrays. Various studies have examined the differences between collocated DAS and geophones or seismometers (Daley *et al.*, 2016; Lindsey *et al.*, 2017; Wang *et al.*, 2018). In this case, the DAS measurement is the most similar to the *Z* axis of the geophone; whereas geophones measure particle velocity, the DAS system in this study measures strain rate along the direction of the fiber. In its simplest form, the difference between strain-rate DAS records and velocity geophone records amounts to one time derivative and scalar multiplication by the local phase velocity. However, direct record comparisons from collocated DAS and geophones can also be complicated by angular sensitivity differences, fiber coupling, and other characteristics of the DAS instrument response. In Figure 5, we show a quantitative comparison between the two measurements for the event shown in Figure 4a, before its filtering. Downhole geophones, in this case, are actually accelerometers, and their naming is a misleading convention. We process the geophone point sensor data by applying a linear detrend, mean removal, and 2% taper to the raw velocity acceleration records before applying a two corner, causal band-pass filter in the range 1–1000 Hz. We

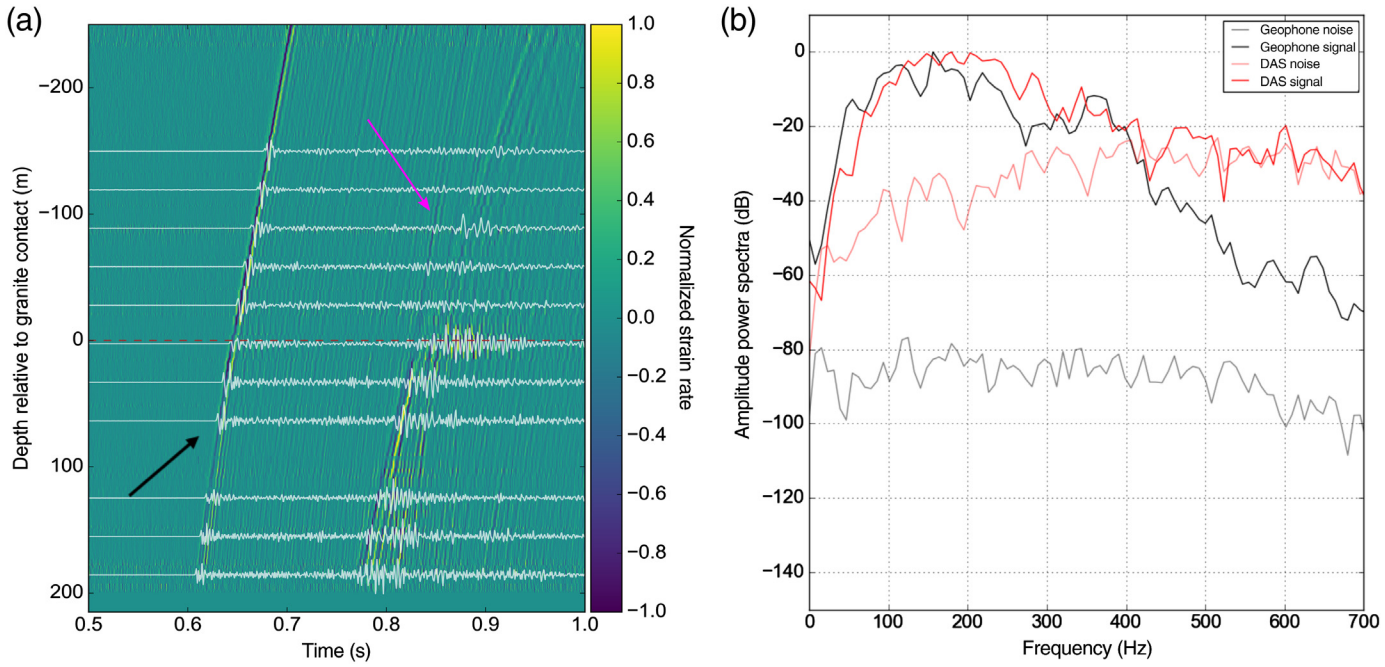


**Figure 5.** (a) DAS strain rate (color image) and geophone acceleration records (white lines) of the microseismic event shown in Figure 4. Both are normalized by the peak trace amplitude. The approximated granite contact is in a dashed brown line. The kinematic agreement is excellent for both *P* and *S* arrivals. An *S*–*P* conversion is clearly visible only in the DAS record (pink arrow). (b) Signal-to-noise comparison for the geophone marked by black arrow in (a) and the collocated DAS channel. Signal and noise were estimated in 0.5 s windows around the earthquake arrival and the time period before the event, respectively. For geophones, the signal (black) is significantly stronger than noise (gray) for a wide frequency range. For DAS, the signal (red) is separated from noise (pink) only between 10 and 400 Hz. Between 100 and 500 Hz, the difference in SNR between the two sensors is about 40 dB in the amplitude power spectra. The color version of this figure is available only in the electronic edition.

process the DAS array data by applying a linear detrend, mean removal, and 2% taper, then removing the zero wavenumber noise in the frequency–wavenumber domain over the full array of sensors installed in the well, before applying a two-corner, causal band-pass filter in the range 1–1000 Hz. Kinematically, geophone and DAS recordings show a high degree of agreement. Both *P* and *S* arrivals are visible in the two record sections. The *S*–*P* event converted at the granite contact is clear only in the DAS record. The main benefit of DAS lies in the extended number of virtual channels. It is approximately 30 times as dense as the geophone array. It offers a much better understanding of the different seismic phases, thanks to our ability to trace them coherently. Nonetheless, comparing individual DAS locations with geophones shows that the latter has a significantly better SNR, owing to the lower geophone self-noise. DAS data overcome their self-noise in a narrower frequency range around 10–400 Hz, but, within that range, DAS SNR is about 40 dB less than geophone SNR.

Capturing the entire wavefield with DAS has a key advantage, which is overlooked if only the SNR is compared on a point-by-point basis. The geophone immediately below the granite contact records a long *S*-wave coda envelope lasting 0.1 s, nearly twice the duration of the other geophone recordings. This observation could be interpreted as spurious, related to instrument defect. The DAS recording, however, shows that this is part of a coherent feature of the wavefield from the granite contact down to approximately 35 m below, spanning several gauge lengths. Explanations for this may be a waveguide effect, interaction of the upgoing *S*-wave energy with the downgoing reflected wavefield from the contact, or poor coupling of all sensors in this part of the well. Similarly, the DAS is able to track the *S*–*P* converted waves above the granite, because it records the wavefield every meter and shows this coherent arrival moveout; the spacing and the low number of geophone sensors above the granite would miss this observation entirely.

The DAS data quality of the FORGE experiment is not as high as in other examples of engineered fibers interrogated by the Carina system (Correa *et al.*, 2017; Naldrett *et al.*, 2020; Verdon *et al.*, 2020). These studies showed that the usage of an engineered fiber in conjunction with the Carina system yielded a clear improvement in SNR. At FORGE, the fiber installation method (cemented outside casing) was ideal for the environment. The only difference in installation known to us is that the optical fiber was inside a metal tubing (fiber in metal tube [FIMT]) before being strapped to the outside of the casing. We do not know the reason for the relatively low quality of the DAS data but concur with the observation that it underperformed.

The gauge length used in this study may also be affecting recorded signals. DAS acquisition does not provide a point strain-rate (or strain) measurement but an average estimation over the gauge length. The simplest representation of the gauge length effect is for a directly upgoing wavefront, in which the wavenumber response is $\frac{\sin(\pi \times k \times \mathrm{GL})}{\pi \times k}$, with $k$ being the wavenumber and GL the gauge length (Dean *et al.*, 2016). In this study, the gauge length is 10 m, and events are reaching the array with a nonzero incidence angle. The effect it has manifests through the relation $f = c \times k$, in which $f$ is the frequency and $c$ is the apparent phase velocity. For wavefronts that propagate non-vertically through the array, the apparent velocity will be higher than the medium velocity. However, as the angles of incidence in this study are at most between 15° and 20°, the apparent velocity is increased by less than 10%. A common rule of thumb is that wavelengths longer than five times the gauge length are unaffected, whereas a wavelength of the gauge length will be averaged to 0 and not measured. Shorter-than-gauge-length wavelengths will be severely distorted and attenuated. In this study, the combination of relatively high frequencies (up to 250 Hz) and low velocities in the sedimentary area yields relatively short wavelengths. For example, a 100 Hz event propagating through shallow *P*-wave velocities of 2000 m/s will be attenuated by 36% due to the gauge length. At 150 Hz, this increases to 59% attenuation, and at 200 Hz, the event will be invisible. For *S* waves, the wavelengths are even shorter, and the gauge length becomes problematic at lower frequencies. However, in practice, the higher frequencies are also attenuated by extrinsic and intrinsic mechanisms in the subsurface, and it is not trivial to separate these losses from the effect of the gauge length. Overall, we do not observe severely detrimental effects due to the gauge length. We did not detect any visible notch in the $f$-$k$ domain, probably as a result of high-frequency attenuation before reaching the low-velocity areas. Because this study is mostly focused on kinematic aspects of the wavefronts, we can effectively treat the gauge length as lowering SNR and limiting the effective frequency range.

In the following sections, we compare detection, location, and magnitude estimation results obtained by DAS and geophones. We do not process the geophone data ourselves and rely on the catalog supplied by the industry contractor. A brief summary of the geophone processing workflow can be found in Moore *et al.* (2019). The final results depend on undisclosed parameter choice, and many of the used methods are proprietary, making results irreproducible.

## DAS Detection

Despite their disadvantage in pointwise SNR comparison with downhole geophone sensors, DAS data can be analyzed with array processing techniques, which significantly improves their detection capabilities. We follow the workflow developed by Lellouch, Yuan, Ellsworth, *et al.* (2019) for event detection, using the *P*-wave velocity model previously estimated from DAS. We also applied a scan with *S*-wave velocity, but all the detected events were already found in the *P*-wave scan. The relative potency of the *P* waves is obvious in the microseismic event we show in Figures 4 and 5, and this property is consistent for the vast majority of events. Probably because of DAS directivity and the near-vertical angle of incidence of incoming microseismic events, the *P*-wave signal is clearer, and *P*-based detection performs significantly better—about four times more detections than for *S* waves. We compare our results to the geophone data catalog. In the studied time period, there are 299 events in the catalog. Our DAS detection algorithm detected a total of 110 events that are within 1.5 s from a catalog event. Because the geophone and DAS clocks were only precise to a single-second resolution, such margins are needed. We did not observe false detections and visually confirmed all DAS detections to be microseismic events.

In Figure 6, we analyze the quality of the DAS-based detection in the context of the geophone catalog. There is a very clear correlation between event magnitude and DAS detectability. DAS detection recovers a catalog that is complete down to a magnitude level of −1.4, determined from the deviation from the Gutenberg–Richter relation at low magnitudes. The geophone-based detection extends this catalog to −1.7. Magnitude ranges will, of course, vary between experiments, but here we have quantified the performance improvement between DAS and downhole geophones. We do not claim that our detection algorithm is optimal. However, we affirm that we are able to approach the industry-grade processing of downhole geophones within an **M** 0.3 completeness difference.

## Event Location and Magnitude Estimation

One of the main limitations of DAS is its uniaxial directional measurement. As a result, for a vertical DAS array, we cannot retrieve the azimuth to the recorded events. Nonetheless, we can estimate event depth and horizontal distance from the array, assuming the *P*- and *S*-wave velocities are known down to the event depth. The angle of incidence, measured in relation to the vertical axis, is a by-product of the detection procedure, which scans for different angles and finds the one optimally aligning the seismic events along the array. Nonetheless, for computational speed, detection is usually performed at a rather coarse angle grid.

For precise event location, it is important to refine the angle search for detected events. We use a 0.25° resolution in the location refinement search. To position the event along the imagined ray exiting the array with the angle of incidence we measured, we can use the *S*-to-*P* time difference. Assuming the *P*- and *S*-wave velocities are known along the path of this ray, this time difference translates to distance from the array. Luckily, the bottom of the array, where we estimated the angle of incidence, is already within the granitic basement.

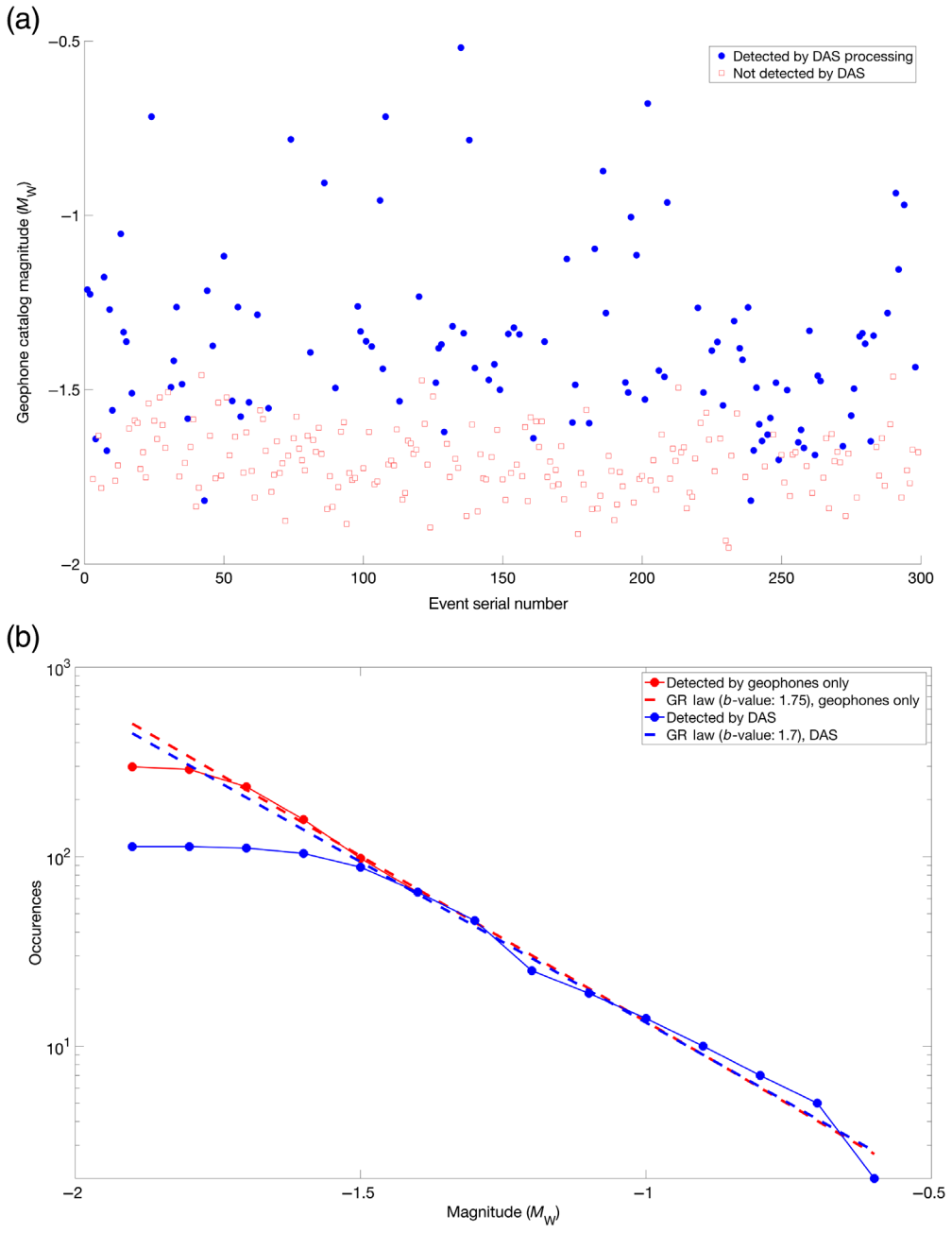


**Figure 6.** (a) DAS detection capabilities. Out of 299 geophone catalog events, 110 are detected by DAS (blue), and 189 are missed (red). All events above a magnitude of −1.4 seem to be detected by DAS. (b) Magnitude completeness and *b*-value estimation using the geophone catalog (red) and DAS detection (blue). The geophone catalog is complete up to approximately −1.7, whereas the DAS detection is complete up to −1.4. Estimated *b*-values are similar when computed within the region of completeness (−1.75 for geophones, dashed red, and −1.7 for DAS, dashed blue). They indicate a stimulation-consistent behavior, dominated by smaller events. GR law, Gutenberg–Richter law. The color version of this figure is available only in the electronic edition.

Therefore, based on the sonic logs in Figure 4, we can reasonably assume constant *P*- and *S*-wave propagation velocities and thus straight-ray propagation. In this case, the distance from the bottom of the array is $t_{SP} \times \frac{V_P \times V_S}{V_P - V_S}$, with $t_{SP}$ being the *S*–*P* time difference, and $V_P = 5715$ m/s, $V_S = 3210$ m/s the average seismic velocities in the granitic basement. These velocities are only used to map the *P* to *S* time difference to distance and represent average properties of the subsurface from the source locations to the bottom of the DAS array, where we record them. To estimate the *S*-arrival time, we apply a moveout correction to the data, using the *S*-wave velocity profile and the angle of arrival estimated from the *P*-wave scan. We find the maximal semblance within 50–300 ms from the *P*-wave arrival time and choose it as the *S*-arrival time. We use events with a semblance of 0.1 and above for both *P* and *S* waves for detection. Forty-five of the 110 DAS detections fulfill this criterion. However, in some events, the maximal semblance did not occur for the first arrival of the *P* or *S* phases, but a later event. As a result, the *S*–*P* time difference was noticeably different, and we manually adjusted the picks to match the right phase. We had to correct the *S*–*P* estimation for about 15% of the events.

There is uncertainty associated with the DAS location process. It arises from errors in the angle of incidence estimation, the *S*–*P* time difference, and the straight-ray propagation assumption. The latter is hard to quantify. From the sonic logs, the velocity up to the depth of the events is very close to constant, but it is only locally true. We do not take this error into account as it is harder to quantify, but it could play an important role. The *S*–*P* time uncertainty can be estimated by the picking error, which depends on the frequency content. Because events reach the bottom of the array with high frequencies (>100 Hz), we estimate that the error is bounded by 10 ms. We estimate the

angular error by analyzing semblance results obtained from different angles. Outside the range of approximately ±2° from the best angle estimation, on average, semblance values drop by 5% or more compared to the maximum. Therefore, we use 2° as an angular error estimation.

In Figure 7, we summarize location results. For DAS events with clear *P* and *S* arrivals, we obtain a very good match with the geophone locations. The possible area of DAS locations taking into account locations errors encapsulates all geophone-derived locations. A direct comparison of DAS and geophone-derived locations shows that DAS locations are horizontally biased toward the well. However, given the uncertainties in the DAS locations, it could also be due to random effects. Interestingly, the events detected by DAS are the ones closest to the stimulation locations. One possible interpretation that we have no way of proving is that DAS reliably detects and locates the stronger events that are associated with the primary fracture openings, close to the stimulation well. Events originating farther away are probably smaller fractures that generate less energy when opening and thus remain unlocated by DAS.

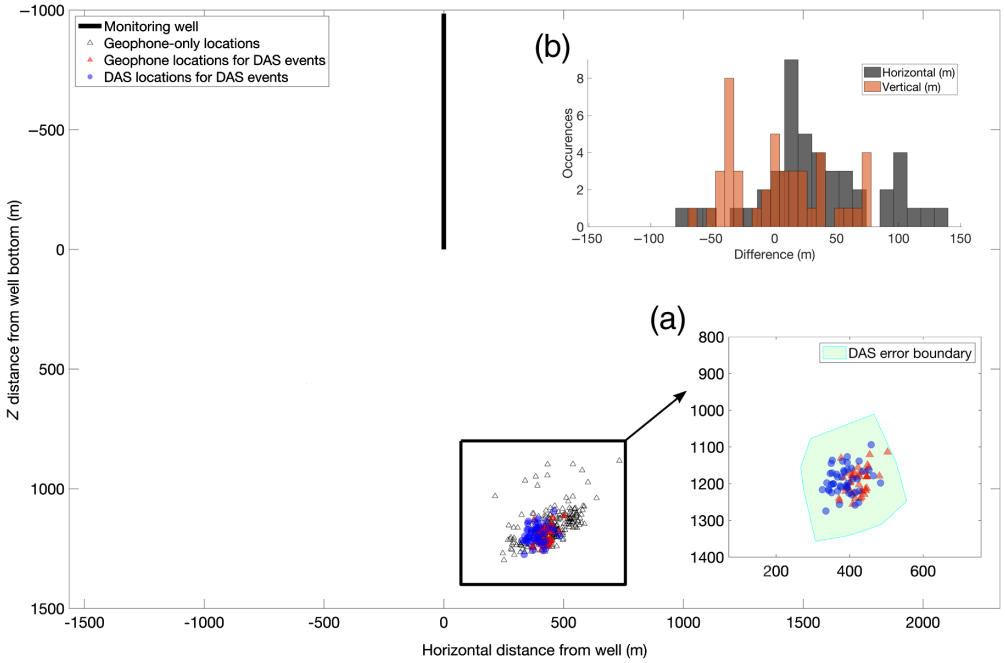


**Figure 7.** DAS-based location. The monitoring well is shown in black. Events are plotted as a function of the horizontal and depth distance from the bottom of the monitoring well. Triangles denote all locations from the geophone catalog, after a projection to the distance–depth plane. Blue circles indicate DAS locations. The projected geophone locations for these events are colored in red. (a) The boxed section, where all events occur, is zoomed on. DAS locations are very close to the geophone-based ones, and the microseismic cloud has similar dimensions. In a green background, we plot the possible locations of all DAS events, taking into account errors in the location process. (b) A histogram depicting the differences between DAS and geophone-based locations. DAS locations are slightly biased toward the well. The color version of this figure is available only in the electronic edition.

Using estimated event distances, we can compute local event magnitudes directly from the DAS data. Assuming a single *Z*-component measurement, we integrate the DAS strain-rate data in time, yielding a strain measurement. We take the maximal strain value from the bottom 100 channels of the DAS array. We also apply a median filter and band-pass filter between 10 and 250 Hz to avoid contamination of our results by optical noise and fading effects. We then use the event distance from the centroid of the bottom 100 channels to estimate the local magnitude using the following equation (after Bullen and Bolt, 1985):

$$M_L = \log_{10}(S \times 10^{-9} \times 10^6 \times \mathrm{GL}) + 2.56 \times \log_{10}(R) - 1.67,$$

in which $M_L$ is the estimated local magnitude, $S$ is the maximum strain measured in nanostrains, GL is the DAS gauge length in meters, and $R$ is the hypocenter-channel distance in kilometers. We show the results in Figure 8. The DAS magnitude estimations are in a generally good agreement with the geophone catalog, with almost no mean error and a standard deviation of $M = 0.115$. Nonetheless, a linear regression between the DAS and geophone magnitudes shows a slope of 1.12 instead of 1, indicating that the DAS magnitude calculation is not perfect. The error associated with our estimation arises from distance uncertainty and noise in the DAS strain measurement. We use the distance uncertainty values discussed earlier in the location analysis. For the strain measurement noise, we take into account both the median of the cumulative strain before the first arrival, which should be zero, and the standard deviation of the maximal strain, measured over the bottom 100 channels. The sum of these two represents noise in the DAS signal and yields the error estimation shown in magenta in Figure 8.

In addition to this uncertainty, there are several inherent limitations to magnitude estimation using DAS that are much more challenging to quantify. First, the uniaxial measurement inherently misses some of the propagating energy. Although

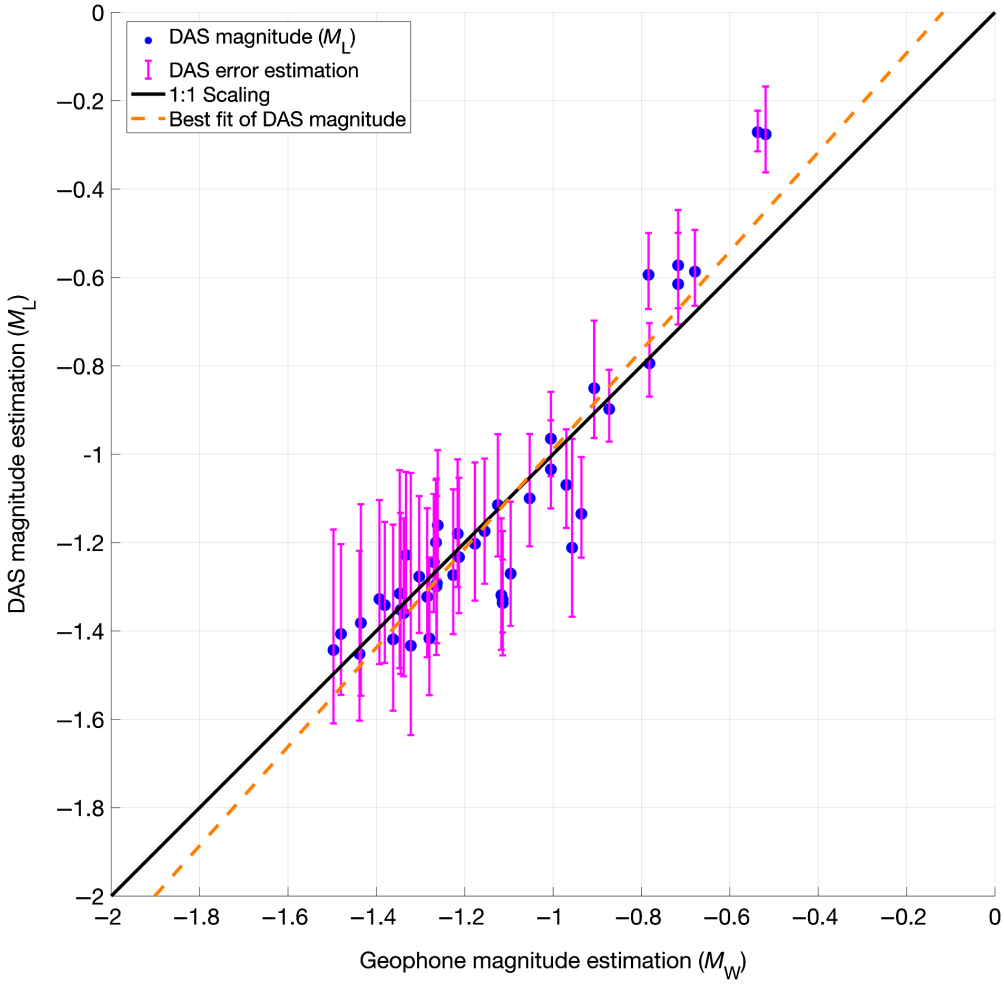


**Figure 8.** DAS local magnitude estimation for located events. Each circle is an event, characterized by both geophone and DAS magnitudes. The error estimation due to noise in the DAS signal is in magenta. The black line indicates a 1:1 scaling between the catalogs. The orange line indicates a linear regression of the data. The correlation coefficient is 0.93, indicating a strong linear correlation between the DAS and the geophone magnitude estimations. However, the slope is 1.12, and not 1. The mean difference in local magnitude units between the two methods is 0.005 ± 0.015 (one standard deviation). The color version of this figure is available only in the electronic edition.

the semiempirical formula we use tries to account for it, it is obviously flawed. For example, two events at the same location and magnitude but different focal mechanisms will yield a different magnitude estimation because of the uniaxial measurement. Second, the previously discussed gauge length effect is not negligible even at the bottom of the array around which the velocities are high. Within the frequency range of interest of up to 250 Hz, the recorded wavenumbers can be as high as 0.08 ($m^{-1}$) for *S*-wave arrivals at the bottom of the array. These frequencies would be attenuated to 25% of their original value using the formula for the gauge length response described earlier. As such, smaller events that generate higher-frequency content may potentially suffer more from the gauge length, and their magnitude will be underestimated. This behavior can be observed in Figure 8, but it might be due to other factors as well. The difference between the moment magnitude ($M_w$) estimated using geophones and the local magnitude ($M_L$) computed from DAS records also influence results. Overall, we conclude that magnitude estimation using DAS is reliable but should be interpreted with caution.

## Discussion and Conclusions

DAS is currently improving many aspects of earthquake seismology and microseismic monitoring, and, as a new technology, data quality is still improving rapidly (Naldrett *et al.*, 2020). DAS arrays offer important practical benefits that this study does not highlight. First, they can be installed in any cased active well, vertical or deviated, even if is being perforated and stimulated (Lellouch, Horne, *et al.*, 2019). As long as the fiber is behind the casing, DAS can eliminate the need for a monitoring well; in the FORGE experiment, a dedicated well was drilled for this purpose. Operating in uncased wells is significantly more challenging. In addition, DAS installations are permanent, and interrogating them for time lapse or intermittent monitoring is simple. Although such acquisition does incur interrogator and data management costs, geophones are much more expensive, as they have to be redeployed in the well. At San Andreas Fault Observatory at Depth, for example, a fiber was successfully used 12 yr after its initial deployment (Lellouch, Yuan, Spica, *et al.*, 2019). Although long-term exposure to high temperatures can degrade fiber quality, DAS arrays can also be deployed in harsh temperature and pressure conditions, in which conventional geophones and seismometers stop functioning quickly. As a result, the DAS array can be much closer to the events of interest, thus significantly improving resolution. Finally, optical fibers can also be used to measure flow, quasistatic strain,

and temperature, although the latter requires a different sensing apparatus. Therefore, although the present microseismic monitoring comparison between DAS and a high-quality geophone array found a slight detectability advantage for the geophone data, future cost-effective EGS monitoring projects will likely favor the DAS for its good recording capability as well as its low cost of downhole equipment, longevity, and added capabilities.

A direct comparison of DAS and geophone-derived location results is not trivial. Because very different processing approaches are employed, all strongly affected by parameter choice, it is unreasonable to expect a perfect agreement between the two. Geophone processing uses the sonic logging velocity, whereas we use the DAS-derived model. The sonic logging covers only a third of the DAS fiber, so this choice if forced. The geophone-based location uses the three different axial components to estimate polarization angles that are taken into account during the location procedure, which is not possible in DAS. Although this is not a fundamental nor necessary difference, the geophone-based location uses raytracing within a 1D sonic-logging velocity model to coherently map events without picking (Moore *et al.*, 2019). For DAS, on the contrary, travel-time picks differences are located through a straight-ray assumption. Although the velocity changes in the granitic basement are minimal, this choice could slightly alter locations. The magnitude estimation is based on different methods, but the most significant difference probably arises from the single axis of measurement for DAS.

This study shows that DAS still has significant shortcomings compared to conventional geophones. The point-by-point comparison, despite its obvious bias, illuminates the lower SNR of DAS. However, the difference in the quality of microseismic monitoring information delivered by the two systems is derived from both sensor performance and data-processing steps. Downhole geophones have been used and studied for decades, and industry contractors offer microseismic monitoring as a routine service. DAS has not reached that point yet. However, we think that the processing workflow we suggest here takes advantage of most of the DAS data, and it is thus reasonable to draw conclusions assuming the majority of the difference is due to the sensor property and performance. Both *P*- and *S*-wave high-resolution velocity models can be directly derived along the DAS array. They can be effectively used for an array-based detection that yields magnitude completeness higher by about **M** 0.3 than the geophone catalog. Although DAS can estimate the depth and horizontal distance from the array as precisely as a geophone array, it cannot resolve the azimuthal component, which is a major shortcoming in microseismic interpretation. Only more elaborate array geometries can resolve the azimuthal uncertainty and allow for a 3D event location. Magnitude estimation with DAS is reliable and can be used when proper care is taken during processing. In this study, focal mechanisms were not inferred from the geophone records. Their estimation with DAS is still a topic of ongoing research, and its feasibility depends very much on the acquisition geometry (Karrenbach *et al.*, 2019). In general, the DAS spatial continuity allows for a much better understanding of the seismic waves propagating in the Earth, which is harder to quantify.

Despite these limitations, the more realistic scenario to compare DAS to is a surface array. Downhole monitoring with geophones is expensive and requires the drilling of a dedicated well. At FORGE, a surface array was also deployed, and a regional network is present. Their joint detection of microseismic events amounted to eight out of the 299 events detected by geophones and 110 detected by DAS. Recent reprocessing of the surface geophone data (Maria Mesimeri and Kristine L. Pankow, personal comm., 2020) improved that number from 8 to 19, which is still much worse than our DAS results. A relatively shallow borehole (300 m deep) suffered from strong platform noise and detected only 16 events. Therefore, assuming the cost of DAS is only its installation in the stimulating well, fiber interrogation, and data storage costs, the added information value compared to surface array deployment is substantial.

## Data and Resources

Both geophone and fiber data have been made openly accessible by the Frontier Observatory for Research in Geothermal Energy (FORGE) project, and scripts for downloading data are available at the U.S. Department of Energy (US DOE) Geothermal Data Repository, along with the geophone catalog. The timing for all detected events and perforation shots can be found at https://github.com/ariellellouch/FORGE/blob/master/DAS_Microseis_Catalog. Information about seismic processing of active surface data is available at http://gdr.openei.org/submissions/1141. All websites were last accessed in June 2020.

## Acknowledgments

The authors are first and foremost thankful to Kristine Pankow, who introduced them to the Frontier Observatory for Research in Geothermal Energy (FORGE) experiment and supported them in accessing the data and auxiliary information. Ariel Lellouch was partially supported by the Israeli Ministry of Energy under the program for postdoctoral scholarships in leading universities. Nathaniel J. Lindsey was supported by the George Thompson Postdoctoral Fellowship.

## References

Becker, M. W., and T. I. Coleman (2019). Distributed acoustic sensing of strain at earth tide frequencies, *Sensors* **19,** no. 9, 1975.

Benioff, H. (1935). A linear strain seismograph, *Bull. Seismol. Soc. Am.* **25,** no. 4, 283–309.

Bullen, K. E., and B. A. Bolt (1985). *An Introduction to the Theory of Seismology*, Cambridge University Press, Cambridge, United Kingdom.

Chalifoux, G. V., and R. B. Logan (2009). Method of preventing hydrogen darkening of optic fibre, *U.S. Patent Number 7561776*, available at https://patents.google.com/patent/US7561776B2/en (last accessed June 2020).

Chambers, K., B. D. E Dando, G. A. Jones, R. Velasco, and S. A. Wilson (2014). Moment tensor migration imaging, *Geophys. Prospect.* **62,** 879–896.

Chambers, K., J. M. Kendall, S. Brandsberg-Dahl, and J. Rueda (2010). Testing the ability of surface arrays to monitor microseismic activity, *Geophys. Prospect.* **58,** 821–830.

Correa, J., A. Egorov, K. Tertyshnikov, A. Bona, R. Pevzner, T. Dean, B. Freifeld, and S. Marshall (2017). Analysis of signal to noise and directivity characteristics of DAS VSP at near and far offsets—A CO2CRC Otway Project data example, *Leading Edge* **36,** 994a1–994a7.

Daley, T. M., D. E. Miller, K. Dodds, P. Cook, and B.M. Freifeld (2016). Field testing of modular borehole monitoring with simultaneous distributed acoustic sensing and geophone vertical seismic profiles at Citronelle, Alabama, *Geophys. Prospect.* **64,** 1318–1334.

Dean, T., T. Cuny, and A. H. Hartog (2016). The effect of gauge length on axially incident *P*-waves measured using fibre optic distributed vibration sensing, *Geophys. Prospect.* **65,** 184–193.

Eisner, L., P. M. Duncan, W. M. Heigl, and W. R. Keller (2009). Uncertainties in passive seismic monitoring, *Leading Edge* **28,** 648–655.

Eisner, L., B. J. Hulsey, P. Duncan, D. Jurick, H. Werner, and W. R. Keller (2010). Comparison of surface and borehole locations of induced seismicity, *Geophys. Prospect.* **58,** 809–820.

Jin, G., and B. Roy (2017) Hydraulic-fracture geometry characterization using low-frequency DAS signal, *Leading Edge* **36,** 975–980.

Karrenbach, M., S. Cole, A. Ridge, K. Boone, D. Kahn, J. Rich, K. Silver, and D. Langton (2019). DAS microseismic, strain and temperature monitoring during hydraulic fracturing, *Geophysics* **84,** D11–D23.

Karrenbach, M., D. Kahn, S. Cole, A. Ridge, K. Boone, J. Rich, K. Silver, and D. Langton (2017). Hydraulic-fracturing-induced strain and microseismic using in situ distributed fiber-optic sensing, *Leading Edge* **36,** 837–844.

Kimura, T., Y. Chen, Y. Kobayashi, Z. Xue, and K. Adachi (2019). DAS VSP acquisition through coiled tubing fiber-optic, *Fifth EAGE Borehole Geophysics Workshop*, The Hague, The Netherlands.

Lellouch, A., S. Horne, M. A. Meadows, S. Farris, T. Nemeth, and B. Biondi (2019). DAS observation of guided waves in a shale reservoir generated by perforation shots, *Leading Edge* **38,** 858–864.

Lellouch, A., S. Yuan, W. L. Ellsworth, and B. Biondi (2019). Velocity-based earthquake detection using downhole distributed acoustic sensing—Examples from the San Andreas Fault Observatory at Depth, *Bull. Seismol. Soc. Am.* **109,** 2491–2500.

Lellouch, A., S. Yuan, Z. Spica, B. Biondi, and W. L. Ellsworth (2019). Seismic velocity estimation using passive downhole distributed acoustic sensing records: Examples from the San Andreas Fault Observatory at Depth, *J. Geophys. Res.* **124,** 6931–6948.

Lim Chen Ning, I., and P. Sava (2018). High-resolution multi-component distributed acoustic sensing, *Geophys. Prospect.* **66,** 1111–1122.

Lindsey, N. J., E. R. Martin, D. S. Dreger, B. Freifeld, S. Cole, S. R. James, B. L. Biondi, and J. B. Ajo-Franklin (2017). Fiber-optic network observations of earthquake wavefields, *Geophys. Res. Lett.* **44,** 792–799.

Lindsey, N. J., H. Rademacher, and J. B. Ajo-Franklin (2020). On the broadband instrument response of fiber-optic DAS arrays, *J. Geophys. Res.* **125,** no. 2, e2019JB018145, doi: 10.1029/2019JB018145.

Majer, E. L., R. Baria, M. Stark, S. Oates, J. Bommer, B. Smith, and H. Asanuma (2007). Induced seismicity associated with enhanced geothermal systems, *Geothermics* **36,** 185–222.

Martin, E. R., N. J. Lindsey, and B. Biondi (2018). Introduction to interferometry of fiber optic strain measurements, *EarthArXiv*, 1–33.

Mateeva, A., J. Lopez, J. Mestayer, P. Wills, B. Cox, D. Kiyashchenko, Z. Yang, W. Berlang, R. Detomo, and S. Grandi (2013). Distributed acoustic sensing for reservoir monitoring with VSP, *Leading Edge* **32,** 3–7.

Mateeva, A., J. Lopez, H. Potters, J. Mestayer, B. Cox, D. Kiyashchenko, P. Wills, S. Grandi, K. Hornman, B. Kuvshinov, *et al.* (2014). Distributed acoustic sensing for reservoir monitoring with vertical seismic profiling, *Geophys. Prospect.* **62,** 679–692.

Maxwell, S. (2014). *Microseismic Imaging of Hydraulic Fracturing: Improved Engineering of Unconventional Shale Reservoirs*, SEG Distinguished Instructor Series No. 17, Society of Exploration Geophysicists, Tulsa, Oklahoma.

Maxwell, S. C., D. G. Raymer, M. J. Williams, and P. Primiero (2012). Tracking microseismic signals from the reservoir to surface, *Leading Edge* **31,** 1300–1308.

Moore, J., S. Simmons, J. McLennan, C. Jones, G. Skowron, P. Wannamaker, G. Nash, C. Hardwick, W. Hurlbut, R. Allis, *et al.* (2019). Utah FORGE: Phase 2C Topical Report, available at https://www.osti.gov/biblio/1578287 (last accessed June 2020).

Naldrett, G., T. Parker, S. Shatalin, and M. Mondanos (2020). High-resolution Carina distributed acoustic fibre-optic sensor for permanent reservoir monitoring and extending the reach into subsea fields, *First Break* **38,** 71–76.

Papp, B., D. Donno, J. E. Martin, and A. H. Hartog (2017). A study of the geophysical response of distributed fibre optic acoustic sensors through laboratory-scale experiments, *Geophys. Prospect.* **65,** 1186–1204.

Parker, T., S. Shatalin, and M. Farhadiroushan (2014). Distributed acoustic sensing—A new tool for seismic applications, *First Break* **32,** 61–69.

Uematsu, Y., Y. Kobayashi, S. Mochiji, and Z. Xue (2019). Improving subsurface images for better reservoir management by CT-DAS-VSP in a production well inshore, *Fifth EAGE Borehole Geophysics Workshop*, The Hague, The Netherlands.

Verdon, J. P., S. A. Horne, A. Clarke, A. L. Stork, A. F. Baird, and J. M. Kendall (2020). Microseismic monitoring using a fiber-optic distributed acoustic sensor array, *Geophysics* **85,** no. 3, KS89–KS99.

Wang, H. F., X. Zeng, D. E Miller, D. Fratta, K. L. Feigl, C. H. Thurber, and R. J. Mellors (2018). Ground motion response to an $M_L$ 4.3 earthquake using co-located distributed acoustic sensing and seismometer arrays, *Geophys. J. Int.* **213,** 2020–2036.

Yilmaz, Ö. (2001) *Seismic Data Analysis*, Society of Exploration Geophysicists, Tulsa, Oklahoma.

Zhang, H., K. Pankow, and W. Stephenson (2019). A Bayesian Monto-Carlo inversion of spatial auto-correlation (SPAC) for near-surface *Vs* structure applied to both broadband and geophone data, *Geophys. J. Int.* **217,** 2056–2070.

Zhidong, C., S. Wang, L. Wei, L. Fei, W. Chong, M. Liuyi, and L. Qing (2019). Application of Walkaway-VSP based on joint observation by DAS and geophones in the Tarim basin, northwest China, *89th SEG Annual International Meeting*, San Antonio, Texas, Expanded Abstracts, 974–978.

**Manuscript received 27 April 2020**
**Published online 19 August 2020**